The Astrophysical Journal Letters, 984:L8 (17pp), 2025 May 1 https://doi.org/10.3847/2041-8213/adc439

exoALMA. III. Line-intensity Modeling and System Property Extraction from Protoplanetary Disks

Andrés F. Izquierdo[1,2,3,30], Jochen Stadler[4], Maria Galloway-Sprietsma[1], Myriam Benisty[4,5], Christophe Pinte[6,7], Jaehan Bae[1], Richard Teague[8], Stefano Facchini[9], Lisa Wölfer[8], Cristiano Longarini[9,10], Pietro Curone[9,11], Sean M. Andrews[12], Marcelo Barraza-Alfaro[8], Gianni Cataldi[13], Nicolás Cuello[6], Ian Czekala[14,15], Daniele Fasano[4], Mario Flock[5], Misato Fukagawa[13], Himanshi Garg[7], Cassandra Hall[16,17,18], Iain Hammond[7], Thomas Hilder[7], Jane Huang[19], John D. Ilee[20], Andrea Isella[21,22], Kazuhiro Kanagawa[23], Geoffroy Lesur[6], Giuseppe Lodato[9], Ryan A. Loomis[24], Ryuta Orihara[23], Daniel J. Price[7], Giovanni Rosotti[9], Leonardo Testi[25], Hsi-Wei Yen[26], Gaylor Wafflard-Fernandez[6], David J. Wilner[12], Andrew J. Winter[4,5], Tomohiro C. Yoshida[13,27], and Brianna Zawadzki[28,29]

[1] Department of Astronomy, University of Florida, Gainesville, FL 32611, USA; andres.izquierdo.c@gmail.com
[2] Leiden Observatory, Leiden University, P.O. Box 9513, NL-2300 RA Leiden, The Netherlands
[3] European Southern Observatory, Karl-Schwarzschild-Str. 2, D-85748 Garching bei München, Germany
[4] Université Côte d'Azur, Observatoire de la Côte d'Azur, CNRS, Laboratoire Lagrange, 06304 Nice, France
[5] Max-Planck Institute for Astronomy (MPIA), Königstuhl 17, 69117 Heidelberg, Germany
[6] Université Grenoble Alpes, CNRS, IPAG, 38000 Grenoble, France
[7] School of Physics and Astronomy, Monash University, Clayton VIC 3800, Australia
[8] Department of Earth, Atmospheric, and Planetary Sciences, Massachusetts Institute of Technology, Cambridge, MA 02139, USA
[9] Dipartimento di Fisica, Università degli Studi di Milano, Via Celoria 16, 20133 Milano, Italy
[10] Institute of Astronomy, University of Cambridge, Madingley Road, CB3 0HA, Cambridge, UK
[11] Departamento de Astronomía, Universidad de Chile, Camino El Observatorio 1515, Las Condes, Santiago, Chile
[12] Center for Astrophysics—Harvard & Smithsonian, Cambridge, MA 02138, USA
[13] National Astronomical Observatory of Japan, 2-21-1 Osawa, Mitaka, Tokyo 181-8588, Japan
[14] Centre for Exoplanet Science, University of St. Andrews, North Haugh, St. Andrews, KY16 9SS, UK
[15] School of Physics & Astronomy, University of St. Andrews, North Haugh, St. Andrews, KY16 9SS, UK
[16] Department of Physics and Astronomy, The University of Georgia, Athens, GA 30602, USA
[17] Center for Simulational Physics, The University of Georgia, Athens, GA 30602, USA
[18] Institute for Artificial Intelligence, The University of Georgia, Athens, GA 30602, USA
[19] Department of Astronomy, Columbia University, 538 W. 120th Street, Pupin Hall, New York, NY, USA
[20] School of Physics and Astronomy, University of Leeds, Leeds, LS2 9JT, UK
[21] Department of Physics and Astronomy, Rice University, 6100 Main Street, Houston, TX 77005, USA
[22] Rice Space Institute, Rice University, 6100 Main Street, Houston, TX 77005, USA
[23] College of Science, Ibaraki University, 2-1-1 Bunkyo, Mito, Ibaraki 310-8512, Japan
[24] National Radio Astronomy Observatory, 520 Edgemont Road, Charlottesville, VA 22903, USA
[25] Dipartimento di Fisica e Astronomia, Università di Bologna, I-40190 Bologna, Italy
[26] Academia Sinica Institute of Astronomy & Astrophysics, 11F of Astronomy-Mathematics Building, AS/NTU, No.1, Sec. 4, Roosevelt Road, Taipei 10617, Taiwan
[27] Department of Astronomical Science, The Graduate University for Advanced Studies, SOKENDAI, 2-21-1 Osawa, Mitaka, Tokyo 181-8588, Japan
[28] Department of Astronomy, Van Vleck Observatory, Wesleyan University, 96 Foss Hill Drive, Middletown, CT 06459, USA
[29] Department of Astronomy & Astrophysics, 525 Davey Laboratory, The Pennsylvania State University, University Park, PA 16802, USA
Received 2024 December 2; revised 2025 February 25; accepted 2025 March 4; published 2025 April 28

Abstract

The ALMA large program exoALMA offers a unique window into the three-dimensional physical and dynamical properties of 15 circumstellar disks where planets may be actively forming. Here, we present an analysis methodology to map the gas disk structure and substructure encoded in ^{12}CO, ^{13}CO, and CS line emission from our targets. To model and characterize the disk structure probed by optically thin species, such as CS and, in some cases, ^{13}CO, we introduce a composite line profile kernel that accounts for increased intensities caused by the projected overlap between the disk's front and back side emission. Our workflow, built on the DISCMINER modeling framework, incorporates an improved iterative two-component fitting method for inclined sources ($i > 40°$) to mitigate the impact of the disk back side on the extraction of velocity maps. Also, we report best-fit parameters for the Keplerian stellar masses, as well as inclinations, position angles, systemic velocities, rotation direction, and emission surfaces of the disks in our sample.

Unified Astronomy Thesaurus concepts: Protoplanetary disks (1300); Exoplanets (498); Planet formation (1241)

1. Introduction

Since the initial reports of candidate planet-driven perturbations in the disks of HD 163296 (C. Pinte et al. 2018b; R. Teague et al. 2018) and HD 97048 (C. Pinte et al. 2019), significant progress has been made in the theoretical and observational understanding of the velocity signatures induced by planets embedded in disks (R. Dong et al. 2019; J. Bae et al.

[30] NASA Hubble Fellowship Program Sagan Fellow.

2021; F. Bollati et al. 2021; A. F. Izquierdo et al. 2021; I. Rabago & Z. Zhu 2021; R. Teague et al. 2021; J. Calcino et al. 2022), and effort has been directed toward recovering these features in a statistically robust manner (A. F. Izquierdo et al. 2022, 2023; J. Stadler et al. 2023). As part of the first planet-hunting campaign at (sub)millimeter wavelengths led by the Atacama Large Millimeter/submillimeter Array (ALMA) large program exoALMA (R. Teague et al. 2025), we build on recent advancements in modeling and analysis of molecular line properties to investigate the physical and dynamical structure of disks and identify gas substructures potentially sculpted by planets in formation.

Our methodology features a guided algorithm for performing two-component fits to line profiles, leading to more precise extraction of velocity maps, and the incorporation of channel-map models for optically thin emission. To illustrate our analysis workflow, we use molecular line data from a subset of the exoALMA targets, specifically the disks of HD 135344B and LkCa 15 as observed in ^{12}CO, ^{13}CO, and CS emission.

The Letter is organized as follows. Section 2 describes the data sets used in this work. Section 3 outlines the methodology for modeling line intensity channels and presents the best-fit model parameters for the disks in the exoALMA sample. Section 4 demonstrates the extraction of line profile observables and their connection to the physical and dynamical structure of our targets. Finally, Section 5 summarizes the results of this study.

2. Data

The data used in this Letter comprise continuum-subtracted fiducial images of ^{12}CO and ^{13}CO $J = 3-2$, and CS $J = 7-6$ line emission, with a circular $0\farcs15$ synthesized beam, as defined in R. Teague et al. (2025). For the source-specific analysis of LkCa 15, high surface brightness sensitivity images with a circular $0\farcs3$ synthesized beam are employed to capture the disk's physical properties over a larger radial extent. Across all data sets, the channel spacing used here is 100 m s^{-1} for ^{12}CO and ^{13}CO images and 200 m s^{-1} for CS. Details on the calibration and imaging procedures are provided in R. Loomis et al. (2025).

3. Modeling Channel Maps

To study the physical and dynamical structure of the disks targeted by exoALMA, we employ the DISCMINER channel-map modeling and analysis framework introduced by A. F. Izquierdo et al. (2021). In this section, we use our fiducial data cubes as input for DISCMINER to generate Keplerian model channel maps for ^{12}CO, ^{13}CO, and CS line emission.

A high degree of substructure is apparent in most exoALMA disks through visual inspection of intensity channels and velocity maps. Figure 1 presents one of our targets, HD 135344B, in ^{12}CO emission, where prominent kinks in intensity (bottom panels) and wiggles in velocity (top left) suggest the presence of substantial deviations from Keplerian rotation across much of the disk extent. Interestingly, some of these perturbations coincide with the dusty ring and arc identified in the Band 7 continuum (top right), suggesting a common origin.

To quantify the amplitude of these substructures, we generate smooth DISCMINER models of the disk emission, which can then be subtracted from the data in a subsequent step. Our models adopt a parametric intensity field which, unless otherwise specified, decreases monotonically with radius, and a Keplerian velocity field with differential rotation as a function of height over the midplane. Although this simplified strategy does not account for the underlying physical structure of the disk and radiation transport, it is well suited for fast parameter exploration and the analysis of large data sets while maintaining a reasonable degree of realism.

Our approach incorporates four sets of parameters that control the projected geometry and intensity distribution of the model channels. The first set are the orientation parameters that determine the projected appearance of the disk on the sky, including inclination i, position angle PA, and offsets from the image center, x_c and y_c. The distance to our sources is fixed to Gaia-derived values as listed in R. Teague et al. (2025). The second set are the velocity parameters that shape the model disk's line-of-sight velocity, that is, Keplerian stellar mass $M_\star$, systemic velocity $\upsilon_{\rm LSRK}$, and rotation direction[33] $\mathrm{sgn}_{\rm rot}$. Figure 2 illustrates our adopted geometric conventions and the projected appearance of a disk with clockwise rotation and positive inclination.

Third set are the surface parameters that dictate the elevation of the upper and lower emission layers relative to the disk midplane for each molecular line, under the assumption that these are confined to a geometrically narrow region. The observed height of these layers is determined by the line optical depth, which depends on the excitation properties and spatial distribution of the molecular tracer in the gas phase. This distribution is influenced by intrinsic factors, such as the freeze-out temperature of the tracer, and extrinsic factors, including the chemical environment, radiation field, disk temperature, density, and dust content (see A. Miotello et al. 2023 for a review).

The last set are the line profile parameters that account for the radial and vertical variations in the shape of the model lines, characterized by the peak intensity I_p, half-line-width at half-power L_w, and line slope, L_s. All free parameters and functional forms of the attributes considered by our models are summarized in Table 1.

To generate model channel maps, the parametric attributes initially mapped in disk cylindrical coordinates, (R, ϕ) and $z(R)$, are first rotated and projected onto the sky plane using the orientation and surface parameters. These on-sky attributes, denoted by primes in the following expression, are then combined into a bell-shaped profile that independently produces the model intensity I_m for the upper and lower emission surfaces as a function of the velocity channel of interest,

$$I_m(\upsilon_{\rm ch}) = I_p^{'}\left(1 + \left|\frac{\upsilon_{\rm ch} - \upsilon_0^{'}}{L_w^{'}}\right|^{2L_s^{'}}\right)^{-1}, \quad (1)$$

where $\upsilon_0^{'}$ is the model line-of-sight velocity, accounting for the Keplerian motion of the disk at the emission surface $z(R)$, projected onto the sky plane, and referred to the systemic velocity of the source, $\upsilon_{\rm LSRK}$.

[33] The sign of the inclination and rotation direction are critical factors when modeling sources where both the front and back sides of the disk contribute to the observed intensity. These properties can be determined by locating the redshifted and blueshifted sides of the disk relative to the central channel—defined by the systemic velocity—and identifying the half of the disk nearest to the observer (or "near side" for short), which is typically indicated by the prominence of the back side of the disk.

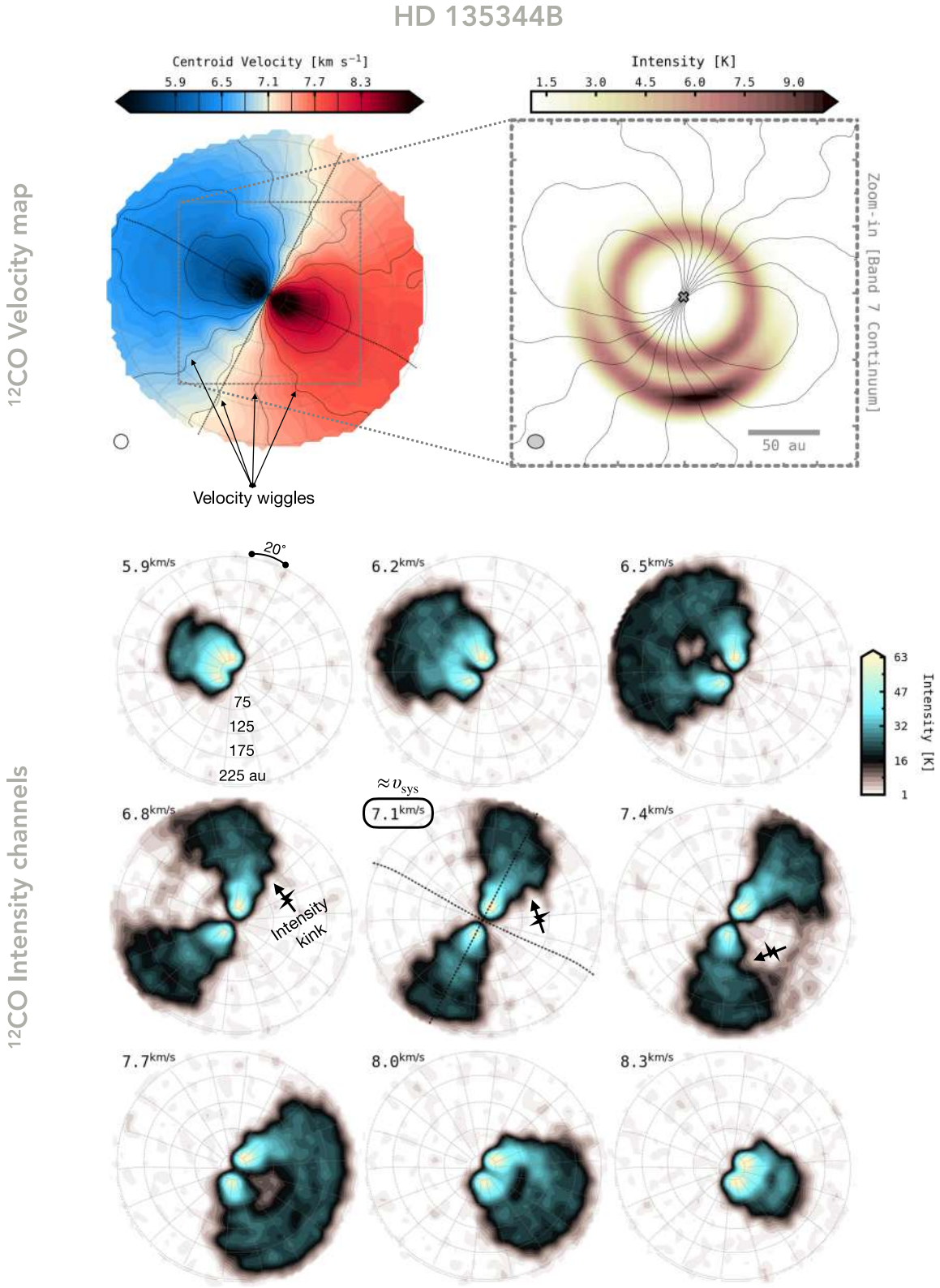

Figure 1. Selected observables from the disk of HD 135344B. Top row: velocity map extracted from the centroid of Gaussian fits to ^{12}CO $J = 3-2$ line intensity profiles. A zoom-in around the center of the target illustrates the Band 7 continuum emission and the coexistence of dust substructures and velocity perturbations. Bottom panels: selected ^{12}CO intensity channels for the same source, converted to brightness temperature using the Rayleigh–Jeans approximation. In all panels, the background grid follows the ^{12}CO emission surface and the best-fit model orientation retrieved by DISCMINER. For reference, arrows mark the location of example intensity kinks identified in the middle row channels (see also C. Pinte et al. 2025 for a discussion).

The choice of this kernel is motivated by its ability to capture the morphology of optically thick lines, such as those originating from ^{12}CO and generally also ^{13}CO emission. These lines typically exhibit a flat intensity profile at the peak and a rapid intensity decay toward the wings (A. Hacar et al. 2016). By introducing one additional parameter—the line

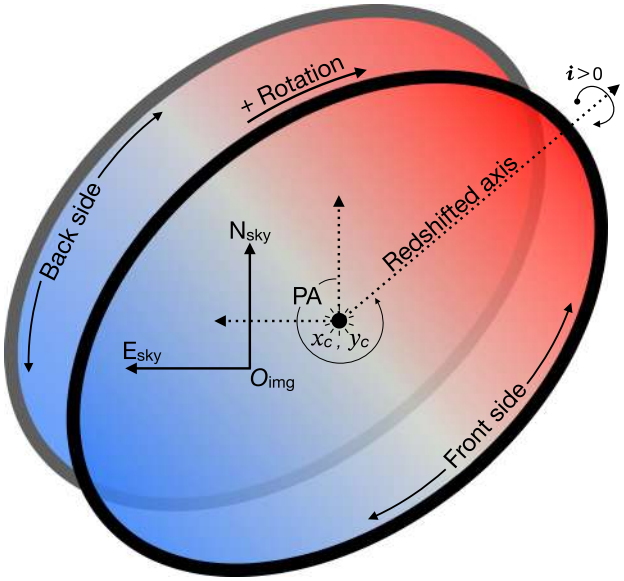

Figure 2. Cartoon illustrating our adopted geometric parameter conventions and the projected rotation velocity of a disk with positive inclination and clockwise rotation.

Table 1
List of Default Attributes and Prescriptions Adopted in Our DISCMINER Models

Attribute	Prescription
Orientation	i, PA, x_c, y_c
Velocity	$v_k = \sqrt{\frac{GM_\star}{r^3}}R$, v_{LSRK}
Upper surface	$z = z_0(R/D_0)^p \exp[-(R/R_t)^q]$
Lower surface	$z = -z_0(R/D_0)^p \exp[-(R/R_t)^q]$
a. Peak intensity	$I_p(R \leqslant R_{out}) = I_0(R/D_0)^p(z/D_0)^q$
b. Peak intensity	$I_p(R \leqslant R_{out}) = I_0(R/R_b)^{p_n}(z/D_0)^q$,
$p_n = \begin{cases} p_1, & \text{if } R \leqslant R_b \\ p_2, & \text{if } R > R_b \end{cases}$	
Line width	$L_w = L_{w0}(R/D_0)^p(z/D_0)^q$
Line slope	$L_s = L_{s0}(R/D_0)^p$

Note. G is the gravitational constant; $D_0 = 100$ au is a normalization factor. In disk coordinates, z is the emission height above the disk midplane, R is the cylindrical radius, and r is the spherical radius. The remaining variables are free parameters. All free parameters are modeled independently. The model intensity is set to zero for radii greater than R_{out}. Disks with strong intensity gradients near the center are modeled using the type b prescription for the peak intensity. This prescription consists of a broken power-law radial profile characterized by the breaking radius R_b.

slope, L_s—the selected kernel outperforms a standard Gaussian in reproducing such profiles. The Bell kernel is also effective for modeling optically thin lines as it approximates a Gaussian profile for low line slopes, as illustrated in Figure 3.

We note that if the optically thin emission is not confined to a geometrically narrow region, the derived surface heights, velocities, and line widths in our model represent an average over multiple disk layers along the line of sight. T. Paneque-Carreño et al. (2024) demonstrated that this layering effect introduces additional nonthermal broadening in optically thin emission from the disk of IM Lup (inclined at $i = 47.^\circ8$) by accounting for the radial and vertical Keplerian

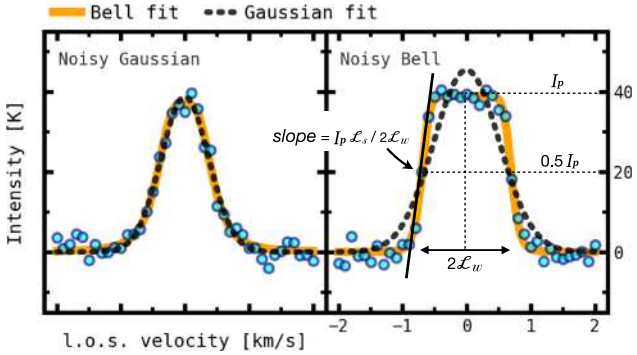

Figure 3. Illustrating Gaussian vs. Bell profiles and their corresponding fits. The profiles are sampled by blue circles every 0.1 km s^{-1}, with an rms noise of 1.4 K, mimicking our fiducial data (see R. Teague et al. 2025). The true amplitude of both profiles is 40 K. The Gaussian width at half-maximum is 0.41 km s^{-1}, which is best fit by a Bell kernel with an amplitude of 38.4 ± 0.9 K, a line width of 0.41 ± 0.01 km s^{-1}, and a line slope of 1.8 ± 0.1. Thus, while the Bell kernel slightly underestimates the Gaussian amplitude, the retrieved width is consistent.

shear set by a stellar mass of $M_\star = 1.1\,M_\odot$. The authors found, however, that even with an assumed emission slab as thick as 50 au, discrepancies between true and retrieved DISCMINER line widths and centroid velocities remain below 30 m s^{-1}. In relation to our data, the optically thinnest of our main tracers, CS, has been suggested to originate from elevations as low as one pressure scale height (A. Dutrey et al. 2017; R. Teague et al. 2022), which aligns with the typical z/r values independently derived for our sources using DISCMINER and DISKSURF (see M. Galloway-Sprietsma et al. 2025 for a comparison). Hence, the thickness of the CS emission region is likely smaller than 50 au across much of the disk extent in most of our targets, minimizing any impact from this layering effect.

To combine the contributions from the front and back sides of the disk to the total line profile, we adopt two strategies depending on the assumed optical depth of the tracer being analyzed. For optically thick emission, we continue using the method introduced in A. F. Izquierdo et al. (2021), which selects the higher intensity between the two components at each pixel and velocity channel. This results in front-side emission dominating when the front- and back-side line profiles are not sufficiently separated in velocity because of projection. For optically thin tracers, however, we now adopt a different approach. In this case, we sum the front- and back-side contributions directly to form the total line profile. By employing these two methods, our models can capture representative features of both optically thick and thin emission, including radial and azimuthal intensity variations arising from overlapping column densities along different lines of sight. Since investigating small-scale changes in the disks' optical depth is beyond the scope of this Letter, we assume either fully optically thick or fully optically thin emission across the entire disk, rather than a combination of both. A mixed assumption would require a transition through a marginally optically thick state, introducing additional free parameters. The impact of using one approach over the other will be illustrated in Section 4.

The modeling library of DISCMINER integrates the EMCEE ensemble sampler for Markov Chain Monte Carlo (D. Foreman-Mackey et al. 2013) to identify the optimal combination of parameters that best matches the observed line intensity of the target disk, I_d, by maximizing the log-likelihood

Table 2
Best-fit Keplerian Stellar Mass, Systemic Velocity, Orientation Parameters, and Rotation Direction Inferred for Our Sources from Fiducial Images of ^{12}CO $J = 3-2$ Line Emission, Which Have a Beam Size of 0.″15 and a Channel Spacing of 100 m s^{-1} (See R. Loomis et al. 2025 and R. Teague et al. 2025 for Details on the Calibration and Imaging Procedures)

Target	$M_\star$ ($M_\odot$)	$\upsilon_{\rm LSRK}$ (km s^{-1})	Rotation ♀ ♌	i (deg)	PA (deg)	x_c (mas)	y_c (mas)	Moment Map Type		
								^{12}CO	^{13}CO	CS
DM Tau	0.45	6.03	+	39.8	335.7	−71.2	−31.4	DB	G	G
AA Tau	0.79	6.50	+	−58.7	272.7	−25.6	47.6	DB	DB	G
LkCa 15	1.17	6.29	−	50.4	61.9	−41.5	50.2	DB	DB	G
HD 34282	1.62	−2.33	+	−58.3	117.4	−12.7	25.3	DB	DB	G
MWC 758	1.40	5.89	+	19.4	240.3	−5.3	48.7	G	G	G
CQ Tau	1.40	6.19	−	−36.3	235.1	−21.5	19.4	G	G	G
SY Cha	0.81	4.10	−	−50.7	345.6	−27.7	37.3	DB	DB	G
PDS 66	1.28	3.96	−	−31.9	189.0	−20.2	19.2	G	G	G
HD 135344B	1.61	7.09	−	−16.1	242.9	−21.0	1.8	G	G	G
HD 143006	1.56	7.72	+	−16.9	168.2	−29.4	26.5	G	G	G
J1604	1.29	4.62	+	6.0	258.1	−78.3	2.3	B	B	G
J1615	1.14	4.75	+	46.1	325.4	−35.9	9.6	DB	DB	G
V4046 Sgr	1.76	2.93	+	−33.6	255.7	−64.1	−38.6	G	G	G
J1842	1.07	5.94	−	39.4	205.9	−19.6	−8.0	DB	G	G
J1852	1.03	5.47	+	−32.7	117.1	−30.1	27.1	G	G	G

Note. Also listed are the fiducial moment map types used for extracting physical properties in this and other Letters in the exoALMA series (see Section 4). Parameter uncertainties are on the order of 0.1%. However, T. Hilder et al. (2025) found that spatially correlated noise can increase these by a factor of ∼10. Moment map abbreviations: DB = double-bell, G = Gaussian, B = Bell.

Table 3
Best-fit Model Emission Surface Parameters Inferred for Our Sources from Fiducial Images of ^{12}CO, ^{13}CO, and CS

Target	Front + Back Side			z_0			p			R_t			q		
	^{12}CO	^{13}CO	CS	^{12}CO (au)	^{13}CO (au)	CS (au)	^{12}CO	^{13}CO	CS	^{12}CO (au)	^{13}CO (au)	CS (au)	^{12}CO	^{13}CO	CS
DM Tau	mask	mask	sum	86.6	21.5	6.5	1.87	2.01	3.17	80	295	94	0.48	1.10	0.92
AA Tau	mask	mask	sum	49.8	51.7	32.9	1.20	1.36	0.83	240	151	232	1.35	1.35	2.18
LkCa 15	mask	sum	sum	29.0	27.3	29.3	1.06	0.87	0.72	795	511	303	3.19	3.46	4.56
HD 34282	mask	mask	sum	34.0	27.2	15.9	1.19	0.79	1.72	512	510	268	3.20	4.41	1.82
MWC 758	mask	⋯	⋯	16.3	66.5	7.6	0.97	3.22	4.96	254	12	111	5.34	0.71	3.29
CQ Tau	mask	⋯	⋯	41.7	38.8	28.0	1.25	1.09	4.59	346	17	80	0.09	0.41	1.53
SY Cha	mask	sum	sum	43.4	72.9	49.7	1.79	2.44	1.92	210	66	124	1.02	0.70	1.75
PDS 66	mask	⋯	⋯	17.4	7.5	1.2	1.83	1.20	2.93	127	29	92	4.48	1.54	8.39
HD 135344B	⋯	⋯	⋯	13.7	10.0	0.0	1.42	1.27	⋯	226	175	⋯	10.0	9.67	⋯
HD 143006	⋯	⋯	⋯	40.5	23.8	16.9	1.89	2.20	0.72	161	146	103	5.98	13.07	4.51
J1604	⋯	⋯	⋯	0.0	0.0	0.0	⋯	⋯	⋯	⋯	⋯	⋯	⋯	⋯	⋯
J1615	mask	mask	sum	26.3	19.0	37.9	1.04	1.04	2.22	530	425	121	6.89	5.92	0.80
V4046 Sgr	mask	mask	⋯	25.9	33.5	0.1	1.84	1.57	0.0	151	66	86	1.17	1.14	7.07
J1842	mask	sum	sum	25.9	17.5	28.6	1.46	1.70	1.43	211	143	145	1.89	2.01	4.46
J1852	mask	mask	sum	75.3	31.2	1.0	1.78	2.74	3.64	61	90	108	0.84	1.33	1.42

Note. The orientation parameters and systemic velocity of the ^{13}CO and CS models were fixed to the ^{12}CO values reported in Table 2. The "Front+Back Side" column indicates how the front- and back-side contributions were combined into a composite model line profile, as detailed in Section 3. For optically thick emission, we use "mask"; for optically thin, we use "sum." Cells with ellipses mark models where the back side does not affect the disk emission symmetry, either due to a near face-on orientation or a shallow vertical structure (see Figures 5 through 9).

function,

$$\log \mathcal{L} = -0.5 \sum_{j}^{n_{\rm ch}} \sum_{i}^{n_{\rm pix}} [I_m(r_i, \upsilon_j) - I_d(r_i, \upsilon_j)]^2 / \sigma_i^2, \qquad (2)$$

where i indexes spatial pixels and j indexes velocity channels. The weighting factor σ_i, is taken as the standard deviation of the observed intensity per pixel, measured from line-free velocity channels.

To sample the parameter space, we adopt flat priors and employ a number of walkers at least 10 times the number of free parameters. These walkers are evolved over an average of 20,000 iterations, allowing them to stabilize around a set of optimal parameters, defined as the median values of the last 10% of the iterations. Tables 2 and 3 summarize the best-fit Keplerian stellar masses, systemic velocities, orientation, and surface parameters derived for all exoALMA disks from the fiducial Images introduced in R. Teague et al. (2025). We refer the reader to C. Longarini et al. (2025) for a summary of the dynamical stellar masses derived from our sources, considering disk pressure and self-gravity forces. In Figure 4, we provide a gallery of the projected vertical structure and rotation velocity of the targets as inferred by our modeling procedure. Parameter uncertainties derived from our posterior distributions for a

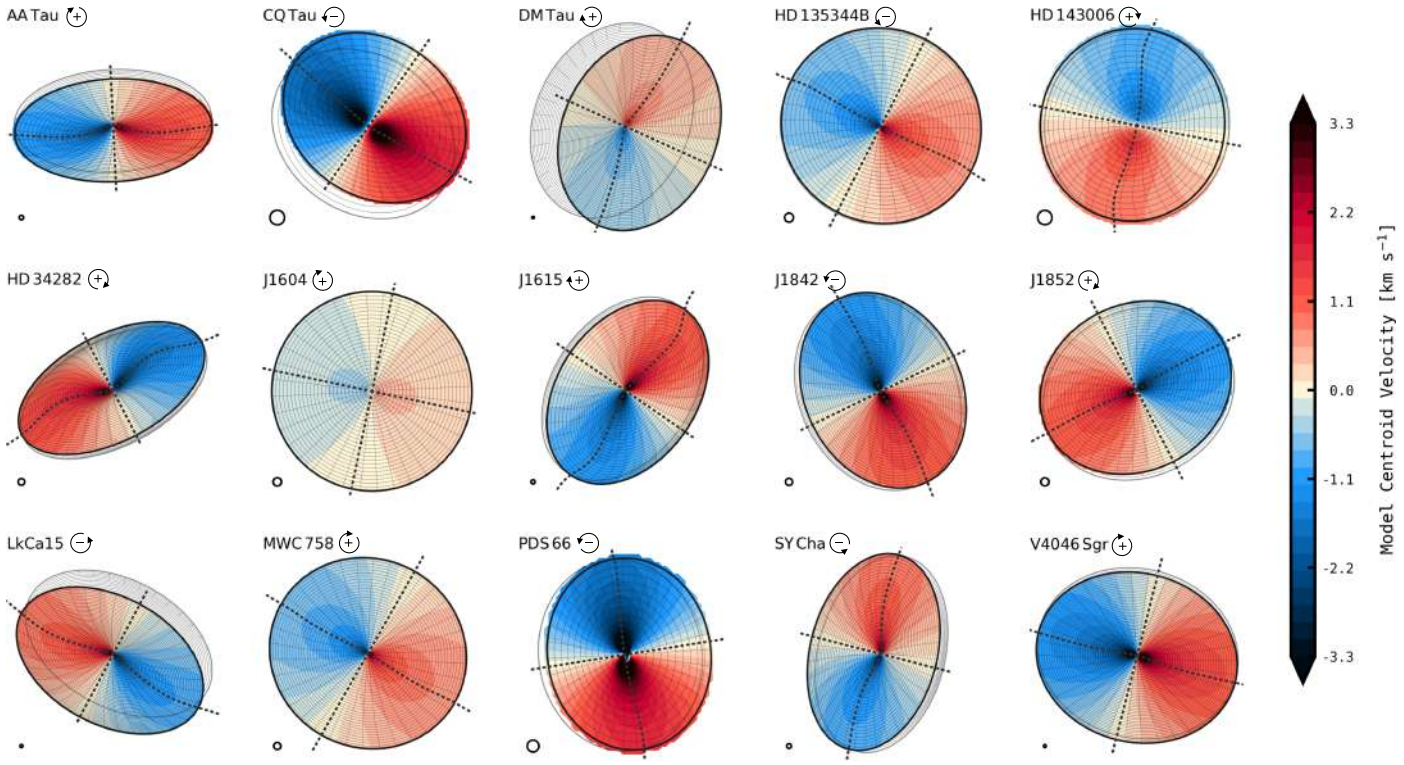

Figure 4. On-sky orientation of the exoALMA targets, illustrating the model vertical structure of the disks and the projected Keplerian rotation of their front sides as inferred with DISCMINER using fiducial images of the ^{12}CO $J = 3-2$ line. The window size is adjusted to match the physical extent of each disk, while the beam size, shown in the lower-left corner, remains fixed at $0\farcs15$. The rotation direction adopted for each disk is noted beside the target names. The outer extent of the modeled back-side structure is also visible when it is sufficiently separated from the front-side outer edge.

mid-inclination source like LkCa 15 ($i = 50\fdg4$) are around 0.1% for the stellar mass and inclination and 0.5% for the upper-surface height normalization z_0. However, our simplified treatment of noise, which neglects correlations between nearby pixels, generally results in underestimated uncertainties. The impact of considering spatial correlations in the noise on our posterior distributions is quantitatively explored in T. Hilder et al. (2025), where more realistic uncertainties are found to increase by a factor of $\sim$10 for velocity, orientation, and surface parameters. For illustration, Figures 11 and 12 in the Appendix present selected intensity channels of ^{12}CO, ^{13}CO, and CS from our observations, along with the best-fit models and the corresponding residuals.

4. Extraction of Moment Maps and Radial Profiles from Line Properties

To identify and quantify perturbations in the physical and dynamical structure of our target disks, we focus on the analysis of variations in the morphological properties of the observed molecular lines, compared to those predicted by the smooth and Keplerian models produced with DISCMINER. In this section, we use the best-fit geometry and velocity parameters derived in Section 3 to demonstrate the extraction of moment maps and radial profiles. The characterization and interpretation of moment map residuals will be presented in upcoming Letters in the exoALMA series.

The morphology of molecular lines emitted by disks, and captured by ALMA, can be complex, particularly when the target is vertically extended and inclined with respect to the observer (see C. Pinte et al. 2023 for a review). This spectral complexity arises primarily from the combined contribution of front- and back-side emission along multiple sight lines and can be further influenced by physical and chemical factors, such as attenuation due to dust content (A. Isella et al. 2018) and velocity-selective absorption through the disk midplane (C. Pinte et al. 2018a; C. P. Dullemond et al. 2020). However, this poses a challenge for conventional methods that rely on single-component profiles to extract molecular line properties and produce moment maps.

Hence, we explore an alternative approach to better characterize the lines targeted by exoALMA. In this section, we demonstrate the necessity of employing two types of extraction methods: single-component and double-component fits applied to the observed and model line profiles. The choice between methods is guided by visual inspection of intensity channels and spectra and is strongly influenced by the disk inclination, emission surface elevation, and the optical depth of the tracer, as these factors dictate how much of the back-side emission contributes to the total line profile. Figure 5 presents a decision tree illustrating this process for the disk of LkCa 15 in ^{12}CO, and Table 3 summarizes our choices for all disks and tracers. For our line profile fits in this step, we use the Levenberg–Marquardt algorithm for least-squares curve fitting, as implemented in the CURVE_FIT module of the SCIPY.OPTIMIZE library.

4.1. Single-peaked Sources

The vertical structure of flat or low-inclination disks (i.e., closer to face-on than to edge-on with respect to the observer) is inherently spatially unresolved. Thus, the line profiles emitted by such sources typically exhibit a single peak, making

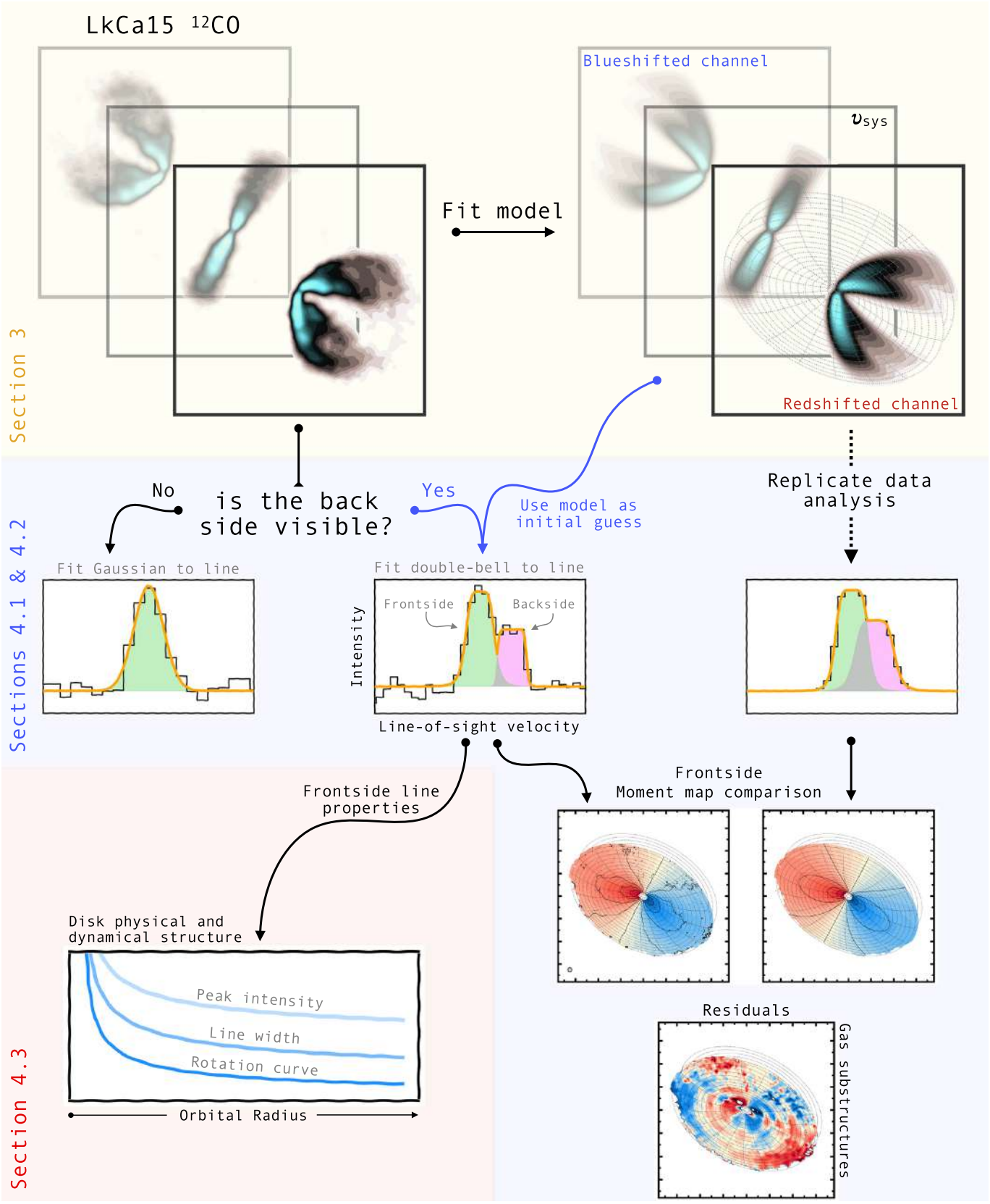

Figure 5. Flowchart illustrating the extraction of line profile properties for ^{12}CO $J = 3-2$ emission from the disk of LkCa 15.

them suitable for fitting with a single-component function like a Gaussian or a Bell profile, as demonstrated in Figure 6 for the ^{12}CO disk of HD 135344B. This constitutes our default approach for deriving moment maps from these specific targets. Among the 15 disks in our sample, and subject to the angular and velocity resolution of our observations, we note

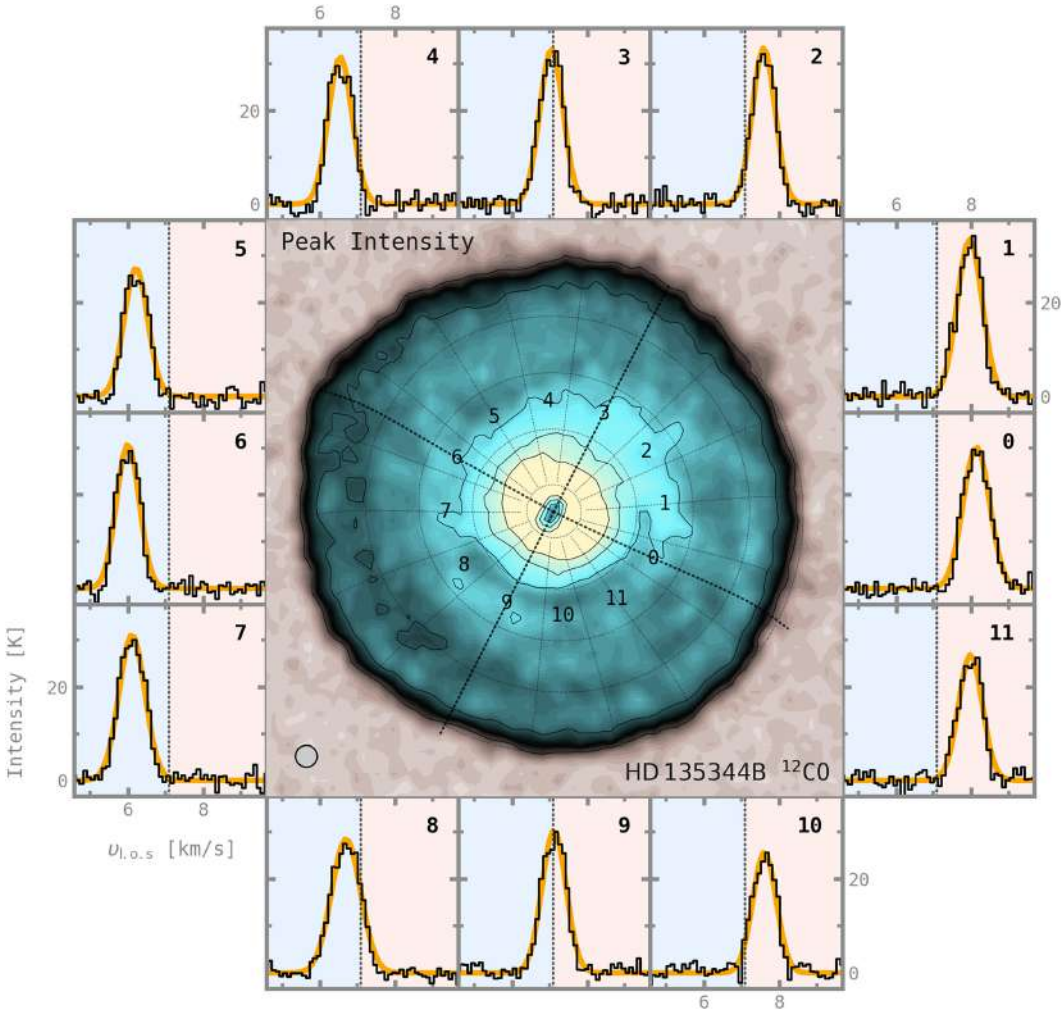

Figure 6. Selected ^{12}CO $J = 3-2$ spectra extracted from the disk of HD 135344B along an annulus at $R = 100$ au, sampled every 30° in the disk frame, at the locations marked by numbers in the central panel, which displays the peak intensity of the disk. The dotted lines in the outer subpanels highlight the systemic velocity of the object. The black solid lines represent the observed spectra, while the orange lines depict the Gaussian fits applied to them. The background of the subpanels is color coded, with red and blue regions indicating the redshifted and blueshifted zones, respectively.

that eight of them fall within this category, all with inclinations smaller than 40°.

The channel maps of a flat single-peaked source could be reproduced by a DISCMINER model using a single emitting surface, the front side of the disk. However, if the target line is optically thin, and the source is sufficiently inclined, this prescription does not necessarily lead to a more accurate representation of the disk intensity and velocity field compared to a two-surface model. In this scenario, even though the observed line profiles may appear single peaked, the contribution from the back side of the disk remains active, and its strength varies from one line of sight to another. This additional emission component becomes evident only after analysis of moment maps and leads to increased peak intensities along the disk minor and major axes, where emission from the front and back sides of the disk adds up due to their proximity in velocity space and significant enhancements in line widths around the disk diagonal axes, where the overlapping front and back sides have the greatest separation in velocity due to projection.

To address this complexity, as explained in Section 3, the DISCMINER models of CS emission from mid- and high-inclination sources incorporate two surfaces that sum in intensity to emulate the effect of overlapping column densities from the front and back sides of the disk. This approach yields a more accurate reproduction of azimuthal features observed in peak intensity and line width maps. Figure 13 in the Appendix demonstrates this for CS emission from the disk of LkCa 15, where a distinct cross pattern appears in the line width map, and elongated intensity patterns become more pronounced along the disk's major and minor axes. The excellent agreement between the "Front+Back" side model and the observed signatures suggests that these features are unlikely to be solely driven by actual density and temperature fluctuations. Instead, they can be attributed to the effects of finite angular resolution and varying optical depth along different sight lines, resulting from the overlapping contributions of front- and back-side emission. This effect is also evident in individual intensity channels, as illustrated in Figure 12 in the Appendix where regions of increased intensity appear where front- and back-side isovelocities intersect or are closely spaced.

4.2. Double-peaked Sources

Mid- and high-inclination disks ($i > 40°$) with line emission originating from elevated surfaces generally exhibit double-peaked spectra. To extract moment maps from these sources,

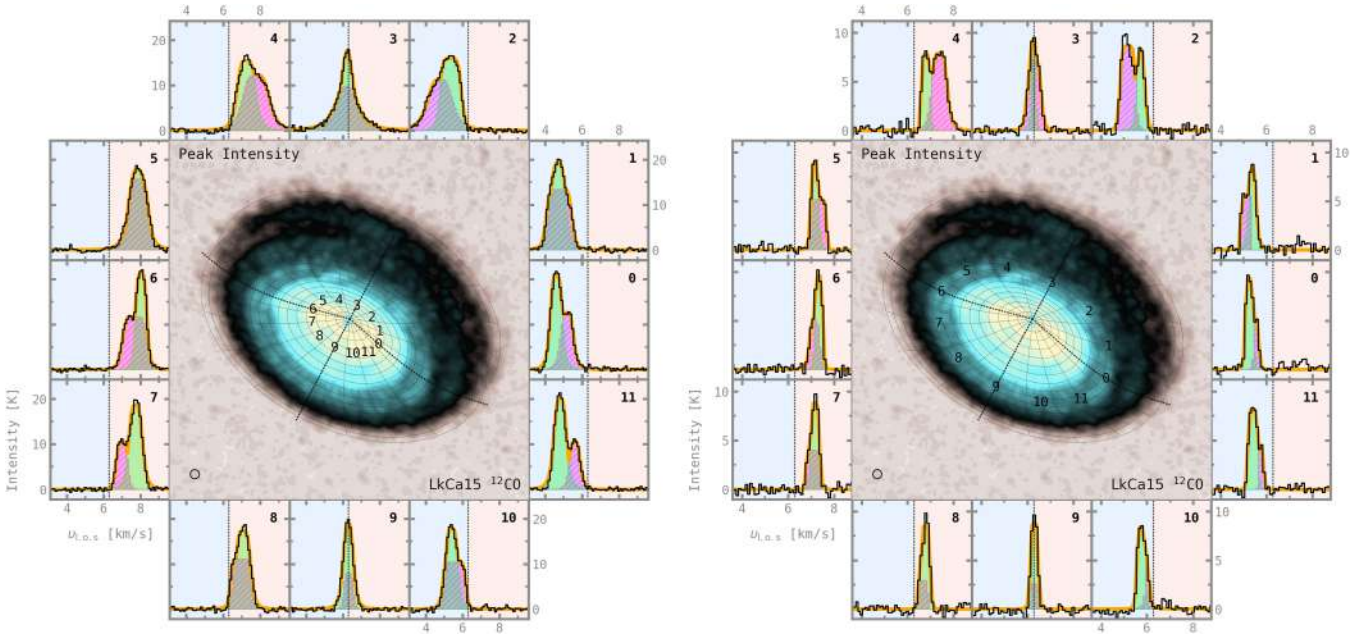

Figure 7. Selected ^{12}CO $J = 3-2$ spectra from the disk of LkCa 15 along annuli at $R = 200$ au (left) and $R = 500$ au (right), sampled every 30° in the disk frame, at the locations marked by numbers in the central panel. The dotted lines in the outer subpanels highlight the systemic velocity of the object. The black solid lines represent the observed spectra, while the orange lines depict the double-bell fits applied to them. Green and magenta shades are also shown within the double-bell fits to illustrate the primary and secondary components of the intensity profile, associated with the front and back sides of the disk, respectively. The background of the subpanels is color coded, with red and blue regions indicating the redshifted and blueshifted zones.

we adopt a default approach that involves fitting a double-bell kernel to the observed line profiles. This fitting procedure is demonstrated in Figure 7 for the ^{12}CO disk around LkCa 15, where line profiles are decomposed into primary (green) and secondary (hatched magenta) components, representing the upper and lower surface contributions to the total intensity, respectively. Unless otherwise specified, we default to using the upper-surface component of this fit to report any subsequent quantities derived from these sources.

Fitting a two-component function to the disk emission can be challenging due to the wide range of velocities and intensities exhibited by these objects (see also S. Casassus et al. 2022; A. F. Izquierdo et al. 2022). To address this, we use the best-fit model obtained with DISCMINER (introduced in Section 3) to provide the CURVE_FIT module with reliable initial guesses for the peak intensity, line width, and centroid velocity of each emission surface in the disk on a per-pixel basis. This approach ensures that the line profile components are naturally assigned to either the front or back side of the disk based on their proximity in velocity and intensity to the corresponding emission surface properties derived from our smooth Keplerian model of the source.

Our algorithm incorporates an iterative routine in which the fit is reattempted for pixels where a single-component is identified or for flagged pixels where (a) neither a double-component nor a single-component fit succeeds, or (b) the fitted line width for either the front or back side is narrower than half the channel width. In each iteration, the fit uses the median parameter values from an 11×11 grid of neighboring pixels, where successful fits were obtained, as new initial guesses. We observe that the number of flagged pixels, which accounts for a small fraction (<10%) of the total, stabilizes after 10 iterations. Figure 8 demonstrates this process for a region of the LkCa 15 disk where the back side is warmer than the front side at the projected location in ^{12}CO emission. Despite this, the algorithm successfully distinguishes between the two components and resolves the flagged pixels appropriately.

Indeed, a key advantage of our model-informed, iterative approach is its capacity to mitigate confusion and prevent the emergence of unphysical substructures caused by projection effects in highly inclined sources, where the back-side contribution to the line profile can often appear brighter than that of the front side in a substantial number of pixels. The ability to separate the front- and back-side components of the line profile significantly improves the precision and accuracy of the resulting velocity maps compared to those derived from methods relying on the line peak velocity or the centroid of Gaussian fits.

To illustrate this, Figure 9 presents a comparison of velocity maps obtained from single- and double-component fits applied to the ^{12}CO $J = 3-2$ line of the LkCa 15 disk, along with the corresponding residuals relative to our DISCMINER model. As depicted in the figure, relying solely on a single-component fit, either quadratic or Gaussian, for this source, leads to contamination from the back side, especially on the near side of the disk where the lower emission surface contributes most prominently because of projection.

4.3. Velocity, Intensity, and Line Width Profiles

We calculate radial profiles of peak intensity, line width, and three disk-frame components of velocity by taking azimuthal averages on the respective moment maps derived from single-peak (Section 4.1) or double-peak fits (Section 4.2) applied to the observed molecular lines.

In cylindrical coordinates, the line-of-sight velocity υ_0 at a point (R, ϕ, z) in the disk can be expressed in its general form as

$$\upsilon_0 = \mathrm{sgn}_{\mathrm{rot}} \cdot \upsilon_\phi \cos\phi \sin i - \upsilon_R \sin\phi \sin i - \upsilon_z \cos i + \upsilon_{\mathrm{LSRK}}, \quad (3)$$

where the inclination i can be negative or positive, $\mathrm{sgn}_{\mathrm{rot}}$ is positive for clockwise rotation (see Section 3 for details), the

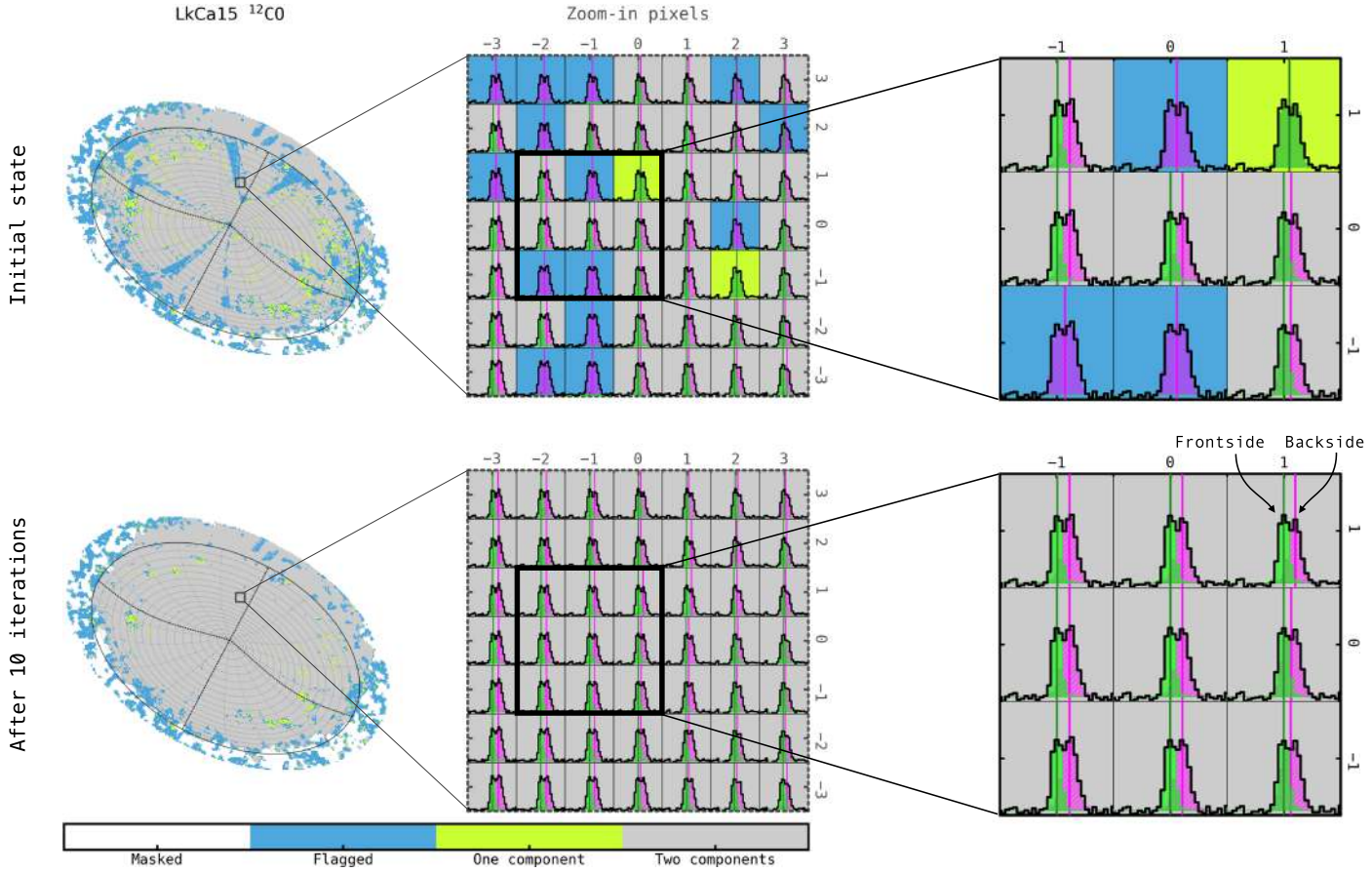

Figure 8. Illustrating the two-component fitting process for a region of the LkCa 15 disk where the back-side ^{12}CO emission is prominent and sometimes dominant. Pixels colored in blue and yellow are refitted using new initial guesses, calculated as the median values of parameters from an 11 × 11 grid of neighboring pixels where the fit was otherwise successful (see Section 4.2). After 10 iterations, the majority of the originally flagged and single-component pixels have converged into a double-component fit, with well-distinguished front- and back-side contributions.

vertical component υ_z is positive for upward flows relative to the midplane, and the radial component υ_R is positive for outward motions relative to the disk center.

These velocity components, however, remain degenerate unless assumptions are made about the symmetry of the velocity field. To compute the rotation velocity component υ_ϕ at a given radial location, we employ the analytical method introduced by A. F. Izquierdo et al. (2023), who demonstrated that if υ_ϕ dominates over υ_z and υ_R, it is proportional to the azimuthal average of the absolute value of the line-of-sight velocity map for an axisymmetric velocity field and can be written as follows:

$$\upsilon_\phi = \frac{\psi}{4 \sin \frac{\psi}{4} \sin|i|} \langle |\upsilon_0 - \upsilon_{\rm LSRK}| \rangle_\psi, \tag{4}$$

where ψ denotes the angular extent of the azimuthal section over which the average is computed and is required to be symmetric with respect to the disk's major axis.

Also, the method states that the vertical velocity component υ_z is proportional to the azimuthal average of the standard velocity map,

$$\upsilon_z = -\frac{1}{\cos i} \langle \upsilon_0 - \upsilon_{\rm LSRK} \rangle_\psi. \tag{5}$$

Finally, we introduce an estimate of the radial velocity component υ_R derived by subtracting the previously computed velocities υ_ϕ and υ_z projected along the line of sight, from the centroid velocity map υ_0 and taking the azimuthal average of the leftover residuals,

$$\upsilon_R = -\langle A_\phi (\upsilon_0 - B_\phi \upsilon_\phi + \upsilon_z \cos i - \upsilon_{\rm LSRK}) \rangle_\psi \tag{6}$$

where $A_\phi = (\sin\phi \sin i)^{-1}$, and $B_\phi = \mathrm{sgn}_{\rm rot} \cos\phi \sin i$.

Employing the double-component moment maps introduced in Section 4.2 for inclined sources allows us to use the entire azimuthal extent of the disk when calculating these averages, thereby reducing the impact of small-scale fluctuations on the rotation, vertical, and radial velocity profiles and enhancing the accuracy of our measurements. In contrast, single-component fits of these sources often require extensive spatial masking to eliminate back-side contamination.

We highlight that the secondary component of the line profiles derived from the double-bell fit (indicated by the hatched magenta profiles in Figure 7) is also helpful as it can be used to extract physical information from the back side of the disk, which is closely linked to the vertical snow line of the molecular tracer (see, e.g., C. Pinte et al. 2018a). This component provides well-constrained peak intensity profiles, which are proxies of the back-side temperature structure, as well as rotation velocities. However, caution is necessary with the latter as our models do not account for absorption from the midplane (see, e.g., C. Pinte et al. 2018a), which may induce fluctuations in the retrieved back-side line widths and centroids that are difficult to predict.

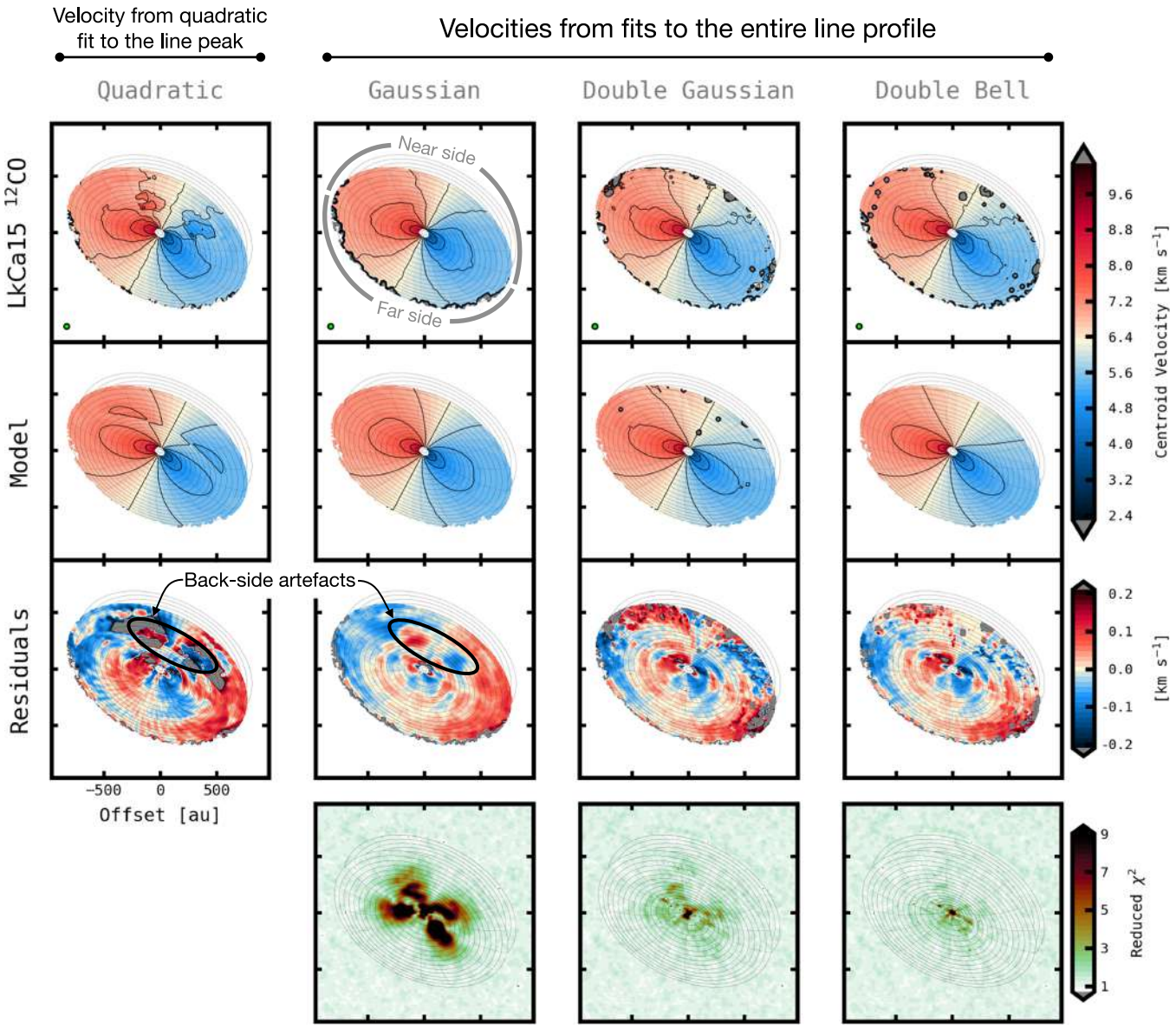

Figure 9. Comparison of velocity maps derived from single- and double-component fits applied to the ^{12}CO line profiles of the disk around LkCa 15. Quadratic fit velocity maps show significant back-side contamination, particularly on the near side of the disk, and are susceptible to channelization effects as they consider a limited number of velocity points around the line peak for fitting, reducing their accuracy. Gaussian moments are accurate but exhibit reduced precision near the disk's diagonal axes due to back-side contamination. Double-component moments are less affected by the back-side contribution, resulting in improved precision in the velocity maps and offering greater accuracy compared to the quadratic method, as they are less influenced by the channel spacing of the datacube. To evaluate the fit quality for the different kernels, the bottom row shows reduced-χ^2 values, calculated as $\chi^2_\nu = (n_{\rm ch} - n_{\rm pars})^{-1}\sum_j^{n_{\rm ch}}(I_{d,j} - I_{m,j})^2/s_j^2$ in the image plane,where s_j is a uniform weighting factor defined as the standard deviation of the observed intensity per channel, measured from line-free pixels.

Figure 10 illustrates the peak intensity, line width, and velocity profiles extracted from ^{12}CO emission for the front side of the disks of HD 135344B and LkCa 15. The peak intensity profiles of both disks show a monotonically decreasing trend, with local variations on the order of a few Kelvin and a typical scale size of $\sim$50 au in radius. A detailed analysis of the three-dimensional temperature structure across all exoALMA disks is presented in M. Galloway-Sprietsma et al. (2025). Additionally, G. Rosotti et al. (2025) estimate the surface densities and masses of these disks by examining their temperatures and CO emission surface heights.

We also note that both disks exhibit rotation velocities that are close to Keplerian, but not perfectly so. Analyses of radial deviations from Keplerian motion across all exoALMA targets are presented in J. Stadler et al. (2025) and C. Longarini et al. (2025), where these variations are linked to modulations in the pressure structure and the self-gravity of the gas disks.

5. Summary

In this Letter, we present a methodology to investigate the radial gas structure and substructure in the 15 protoplanetary disks targeted by the ALMA large program exoALMA. Our approach is based on the DISCMINER modeling framework and incorporates an improved iterative two-component fitting routine devised for inclined sources, allowing us to separate the contribution of the disks' front and back sides to the total intensity profile, which is crucial for a precise characterization of the dynamical and physical structure of our sources. We report best-fit parameters describing the orientation and vertical

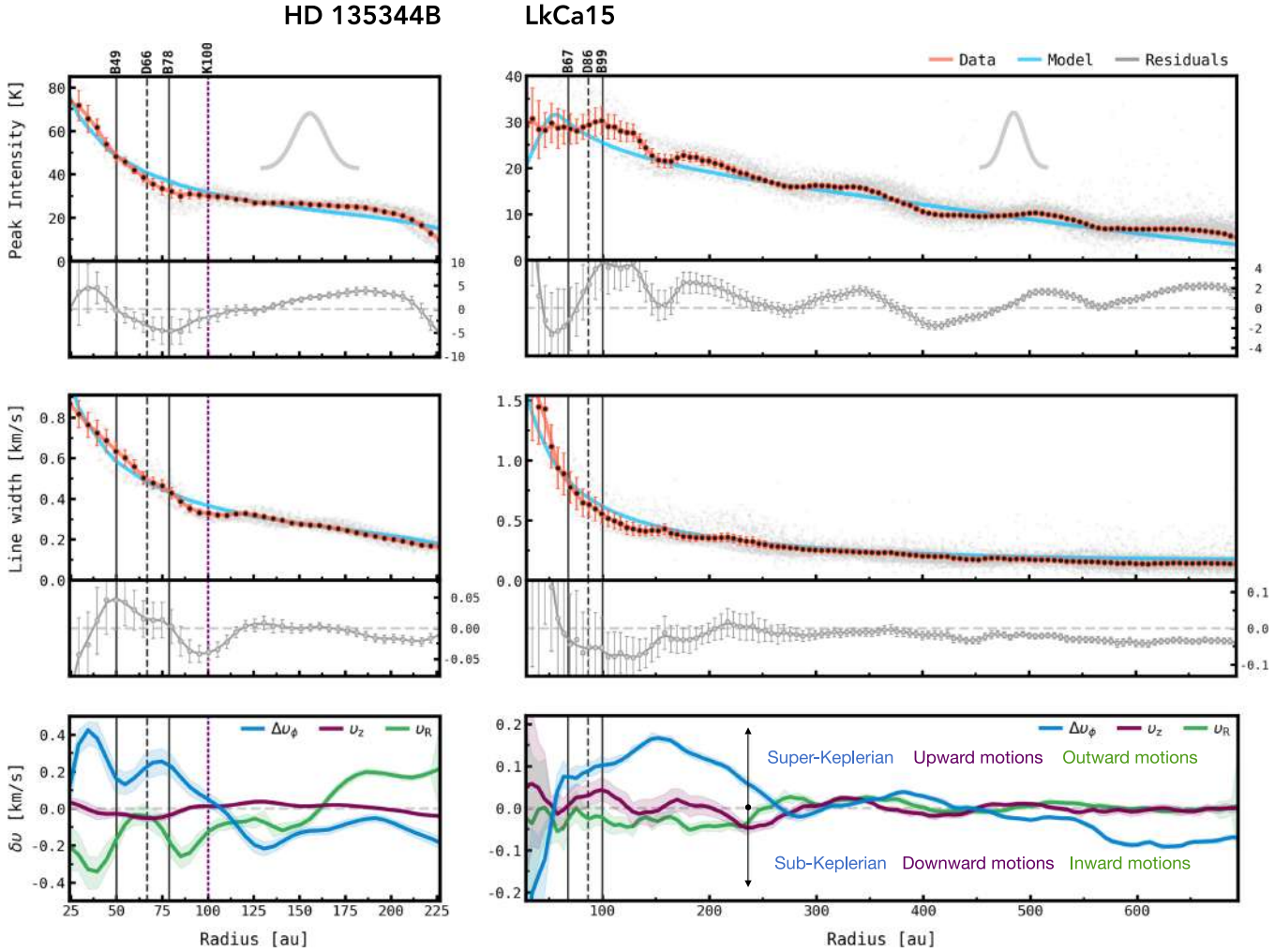

Figure 10. Peak intensity (top), line width (middle), and velocity profiles (bottom) extracted from ^{12}CO $J = 3-2$ emission for the front side of the disks of HD 135344B and LkCa 15, both imaged with a 0.″15 beam, compared to the best-fit model quantities obtained with DISCMINER. The physical size of the beam's major axis is shown as a gray Gaussian profile in the top panels. Vertical lines indicate the radial locations of gaps (D) and rings (B) identified in the millimeter continuum by P. Curone et al. (2025). Peak intensities have been converted to brightness temperature units via the Rayleigh–Jeans approximation. Error bars in the top panels and shaded regions in the bottom panels represent the standard deviation divided by the square root of the number of independent beams along each projected annulus. Gray points in the background of the peak intensity and line width profiles represent values extracted from all pixels in the image, mapped into the disk frame.

structure of our targets, along with Keplerian stellar masses, which serve as a foundation for subsequent analysis Letters in the exoALMA series. Our study underscores the critical role of high-quality data and meticulous examination of molecular line profiles in advancing our understanding of protoplanetary disk physics and dynamics.

Acknowledgments

We thank the anonymous referee for their comments and suggestions, which greatly improved the quality of this work. This Letter makes use of the following ALMA data: ADS/JAO.ALMA#2021.1.01123.L. ALMA is a partnership of ESO (representing its member states), NSF (USA) and NINS (Japan), together with NRC (Canada), MOST and ASIAA (Taiwan), and KASI (Republic of Korea), in cooperation with the Republic of Chile. The Joint ALMA Observatory is operated by ESO, AUI/NRAO and NAOJ. The National Radio Astronomy Observatory is a facility of the National Science Foundation operated under cooperative agreement by Associated Universities, Inc. We thank the North American ALMA Science Center (NAASC) for their generous support including providing computing facilities and financial support for student attendance at workshops and publications. Support for AFI was provided by NASA through the NASA Hubble Fellowship grant No. HST-HF2-51532.001-A awarded by the Space Telescope Science Institute, which is operated by the Association of Universities for Research in Astronomy, Inc., for NASA, under contract NAS5-26555. J.S., M.B., D.F. have received funding from the European Research Council (ERC) under the European Union's Horizon 2020 research and innovation program (PROTOPLANETS, grant agreement No. 101002188). Computations by J.S. have been performed on the "Mesocentre SIGAMM" machine, hosted by Observatoire de la Cote d'Azur. C.P. acknowledges Australian Research Council funding via FT170100040, DP18010423, DP220103767, and DP240103290. J.B. acknowledges support from NASA XRP grant No. 80NSSC23K1312. S.F. is funded by the European Union (ERC, UNVEIL, 101076613), and acknowledges financial contribution from PRIN-MUR 2022YP5ACE. C.L. has received funding from the European Union's Horizon 2020 research and innovation program under the Marie Sklodowska-Curie grant agreement No. 823823 (DUSTBUSTERS) and by

the UK Science and Technology research Council (STFC) via the consolidated grant ST/W000997/1. P.C. and L.T. acknowledge support by the Italian Ministero dell'Istruzione, Università e Ricerca through the grant Progetti Premiali 2012—iALMA (CUP C52I13000140001) and by the ANID BASAL project FB210003. N.C. has received funding from the European Research Council (ERC) under the European Union Horizon Europe research and innovation program (grant agreement No. 101042275, project Stellar-MADE). M.F. has received funding from the European Research Council (ERC) under the European Unions Horizon 2020 research and innovation program (grant agreement No. 757957). M.F. is supported by a Grant-in-Aid from the Japan Society for the Promotion of Science (KAKENHI: No. JP22H01274). C.H. acknowledges support from NSF AAG grant No. 2407679. I.H. and T.H. are supported by an Australian Government Research Training Program (RTP) Scholarship. J.D.I. acknowledges support from an STFC Ernest Rutherford Fellowship (ST/W004119/1) and a University Academic Fellowship from the University of Leeds. A.I. acknowledges support from the National Aeronautics and Space Administration under grant No. 80NSSC18K0828. G.L. has received funding from the European Union's Horizon 2020 research and innovation program under the Marie Sklodowska-Curie grant agreement No. 823823 (DUSTBUSTERS). D.P. acknowledges Australian Research Council funding via DP18010423, DP220103767, and DP240103290. G.R. acknowledges funding from the Fondazione Cariplo, grant No. 2022-1217, and the European Research Council (ERC) under the European Union's Horizon Europe Research & Innovation Programme under grant agreement No. 101039651 (DiscEvol). H.-W.Y. acknowledges support from National Science and Technology Council (NSTC) in Taiwan through grant NSTC 113-2112-M-001-035- and from the Academia Sinica Career Development Award (AS-CDA-111-M03). G.W.F. acknowledges support from the European Research Council (ERC) under the European Union Horizon 2020 research and innovation program (grant agreement No. 815559 (MHDiscs)). G.W.F. was granted access to the HPC resources of IDRIS under the allocation A0120402231 made by GENCI. A.J.W. has received funding from the European Union's Horizon 2020 research and innovation program under the Marie Skłodowska-Curie grant agreement No. 101104656. T.C.Y. acknowledges support by Grant-in-Aid for JSPS Fellows JP23KJ1008. Support for B.Z. was provided by The Brinson Foundation. This work was partly supported by the Deutsche Forschungsgemein- schaft (DFG, German Research Foundation)—Ref no. 325594231 FOR 2634/2 TE 1024/2-1, and by the DFG Cluster of Excellence Origins (www.origins-cluster.de). This project has received funding from the European Research Council (ERC) via the ERC Synergy Grant ECOGAL (grant 855130). Views and opinions expressed by ERC-funded scientists are, however, those of the author(s) only and do not necessarily reflect those of the European Union or the European Research Council. Neither the European Union nor the granting authority can be held responsible for them.

Software: ASTROPY (Astropy Collaboration et al. 2022), CASA (CASA Team et al. 2022), CMASHER (E. van der Velden 2020), DISCMINER (A. F. Izquierdo et al. 2021), EMCEE (D. Foreman-Mackey et al. 2013), MATPLOTLIB (J. D. Hunter 2007), NUMPY (C. R. Harris et al. 2020), SCIKIT-IMAGE (S. van der Walt et al. 2014), SCIPY (P. Virtanen et al. 2020), RADIO-BEAM (E. Koch et al. 2021), SPECTRAL-CUBE (A. Ginsburg et al. 2019).

Appendix
Supporting Figures

In this Appendix, we provide additional figures to support the discussions in Sections 3 and 4. Figures 11 and 12 show selected intensity channels of ^{12}CO, ^{13}CO, and CS for HD 135344B and LkCa 15, along with the corresponding best-fit models and residuals. Figure 13 compares intensity and line width residuals in CS emission for the LkCa 15 disk, contrasting front side–only and front+back side models and motivating our choice of the latter.

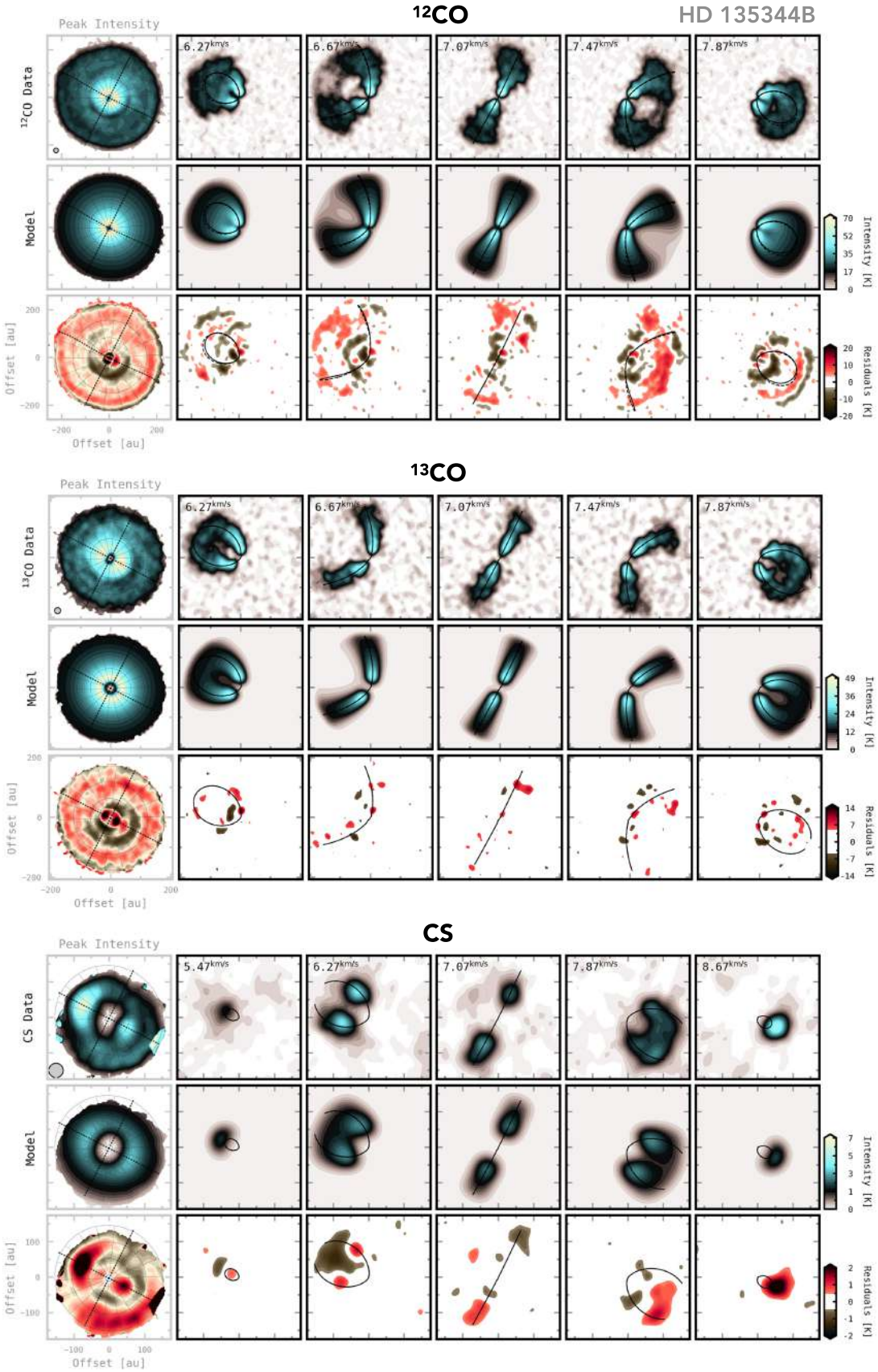

Figure 11. Selected ^{12}CO (top), ^{13}CO (middle), and CS (bottom) intensity channels for the disk of HD 135344B. Each panel displays, from top to bottom, the channel maps for the data, the best-fit model, and the corresponding residuals, with residuals below 3 times the rms noise whited out. Peak intensity maps and residuals are shown in the leftmost column of each panel. Solid and dashed lines overlaid on the channel maps represent isovelocity contours from the model's front and back sides.

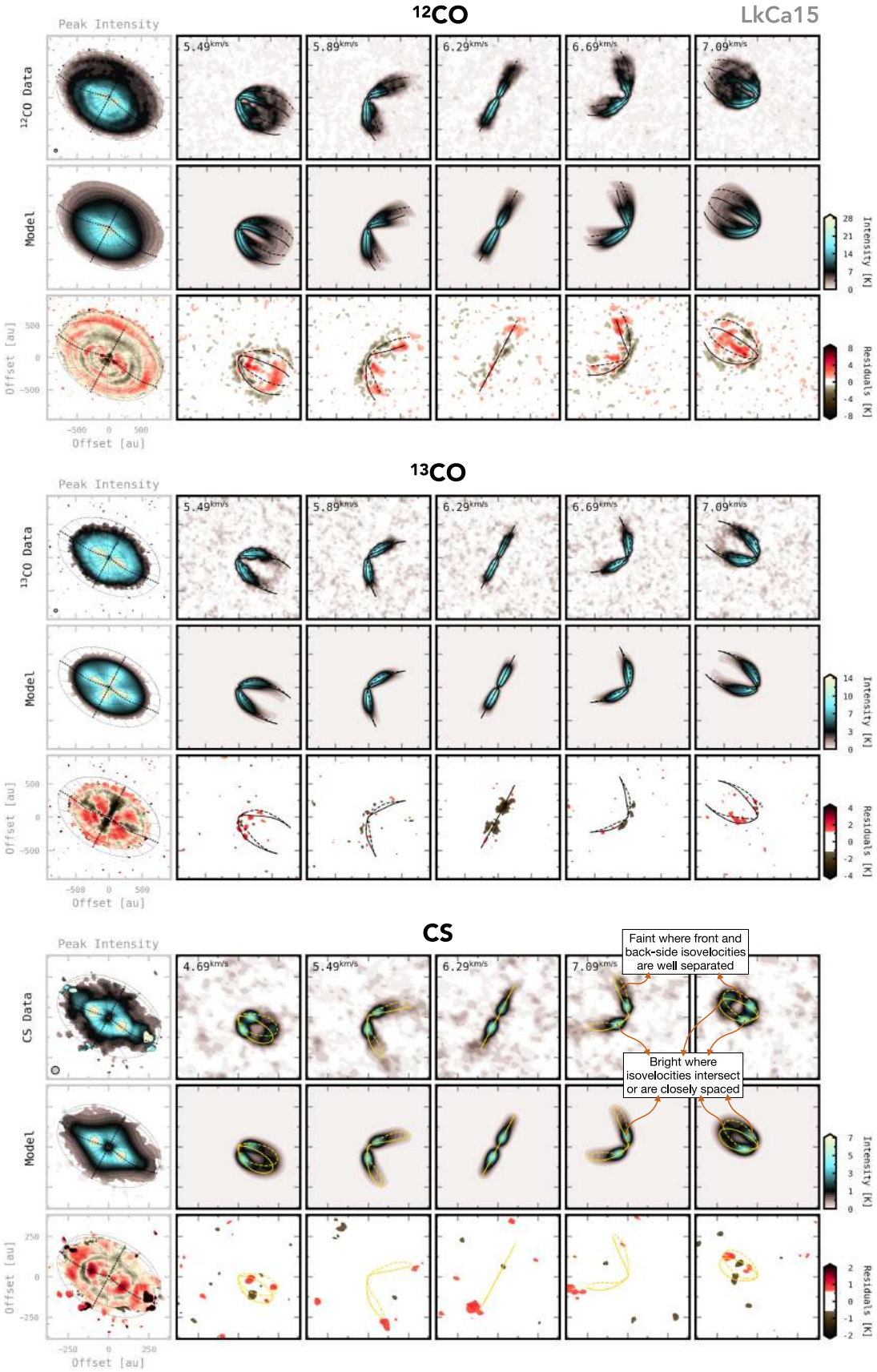

Figure 12. Same as Figure 11 but for the disk of LkCa 15. The ^{13}CO and CS models are assumed to be optically thin and therefore use a "sum" kernel to combine the contributions of the front and back sides to the total intensity (see Sections 3 and 4.1 for details). CS isovelocity contours are shown in yellow to highlight regions where increased intensity results from overlapping column densities of the front and back sides at matching line-of-sight velocities.

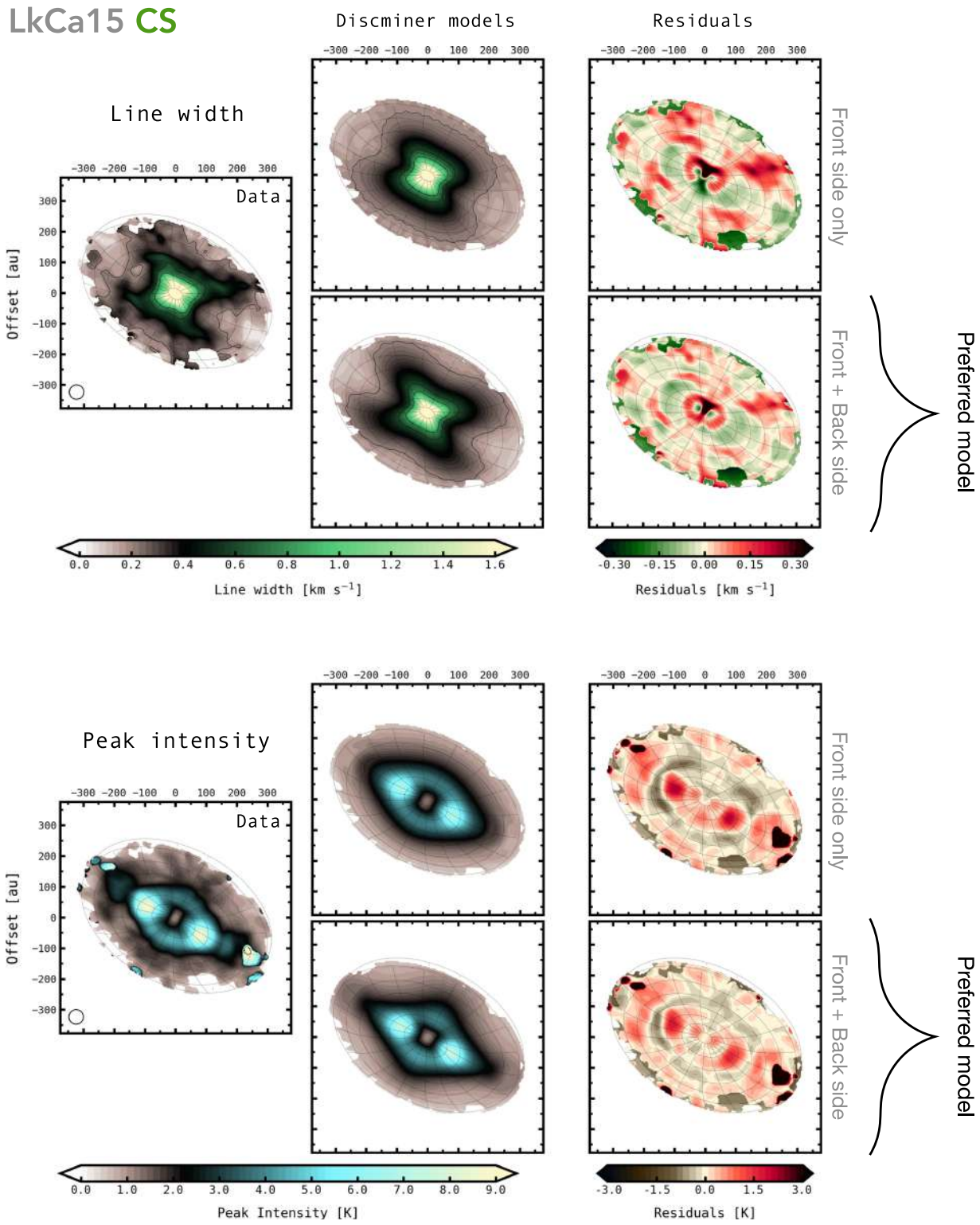

Figure 13. Comparison of line width and peak intensity residuals obtained from CS $J = 7-6$ emission for the disk of LkCa 15 using two models. The first model (top rows) considers only the contribution of the upper surface to the total intensity profile, while the second model (bottom rows) incorporates the summed contribution from both upper and lower emission surfaces. The latter model provides a better reproduction of line width signatures along the disk's diagonal axes and intensity features along the disk's main axes, which result in lower line width and intensity residuals as illustrated in the rightmost panels.

ORCID iDs

Andrés F. Izquierdo https://orcid.org/0000-0001-8446-3026
Jochen Stadler https://orcid.org/0000-0002-0491-143X
Maria Galloway-Sprietsma https://orcid.org/0000-0002-5503-5476
Myriam Benisty https://orcid.org/0000-0002-7695-7605
Christophe Pinte https://orcid.org/0000-0001-5907-5179
Jaehan Bae https://orcid.org/0000-0001-7258-770X
Richard Teague https://orcid.org/0000-0003-1534-5186
Stefano Facchini https://orcid.org/0000-0003-4689-2684
Lisa Wölfer https://orcid.org/0000-0002-7212-2416
Cristiano Longarini https://orcid.org/0000-0003-4663-0318
Pietro Curone https://orcid.org/0000-0003-2045-2154
Sean M. Andrews https://orcid.org/0000-0003-2253-2270
Marcelo Barraza-Alfaro https://orcid.org/0000-0001-6378-7873
Gianni Cataldi https://orcid.org/0000-0002-2700-9676
Nicolás Cuello https://orcid.org/0000-0003-3713-8073
Ian Czekala https://orcid.org/0000-0002-1483-8811
Daniele Fasano https://orcid.org/0000-0003-4679-4072
Mario Flock https://orcid.org/0000-0002-9298-3029
Misato Fukagawa https://orcid.org/0000-0003-1117-9213
Himanshi Garg https://orcid.org/0000-0002-5910-4598
Cassandra Hall https://orcid.org/0000-0002-8138-0425
Iain Hammond https://orcid.org/0000-0003-1502-4315
Thomas Hilder https://orcid.org/0000-0001-7641-5235
Jane Huang https://orcid.org/0000-0001-6947-6072
John D. Ilee https://orcid.org/0000-0003-1008-1142
Andrea Isella https://orcid.org/0000-0001-8061-2207
Kazuhiro Kanagawa https://orcid.org/0000-0001-7235-2417
Geoffroy Lesur https://orcid.org/0000-0002-8896-9435
Giuseppe Lodato https://orcid.org/0000-0002-2357-7692
Ryan A. Loomis https://orcid.org/0000-0002-8932-1219
Ryuta Orihara https://orcid.org/0000-0003-4039-8933
Daniel J. Price https://orcid.org/0000-0002-4716-4235
Giovanni Rosotti https://orcid.org/0000-0003-4853-5736
Leonardo Testi https://orcid.org/0000-0003-1859-3070
Hsi-Wei Yen https://orcid.org/0000-0003-1412-893X
Gaylor Wafflard-Fernandez https://orcid.org/0000-0002-3468-9577
David J. Wilner https://orcid.org/0000-0003-1526-7587
Andrew J. Winter https://orcid.org/0000-0002-7501-9801
Tomohiro C. Yoshida https://orcid.org/0000-0001-8002-8473
Brianna Zawadzki https://orcid.org/0000-0001-9319-1296

References

Astropy Collaboration, Price-Whelan, A. M., Lim, P. L., et al. 2022, ApJ, 935, 167
Bae, J., Teague, R., & Zhu, Z. 2021, ApJ, 912, 56
Bollati, F., Lodato, G., Price, D. J., & Pinte, C. 2021, MNRAS, 504, 5444
Calcino, J., Hilder, T., Price, D. J., et al. 2022, ApJL, 929, L25
CASA Team, Bean, B., Bhatnagar, S., et al. 2022, PASP, 134, 114501
Casassus, S., Cárcamo, M., Hales, A., Weber, P., & Dent, B. 2022, ApJL, 933, L4
Curone, P., Facchini, S., Andrews, S. M., et al. 2025, ApJL, 984, L8
Dong, R., Liu, S.-Y., & Fung, J. 2019, ApJ, 870, 72
Dullemond, C. P., Isella, A., Andrews, S. M., Skobleva, I., & Dzyurkevich, N. 2020, A&A, 633, A137
Dutrey, A., Guilloteau, S., Piétu, V., et al. 2017, A&A, 607, A130
Foreman-Mackey, D., Hogg, D. W., Lang, D., & Goodman, J. 2013, PASP, 125, 306
Galloway-Sprietsma, M., Bae, J., Izquierdo, A., et al. 2025, ApJL, 984, L10
Ginsburg, A., Koch, E., & Robitaille, T. 2019, radio-astro-tools/spectral-cube: Release v0.4.5, Zenodo, doi:10.5281/zenodo.3558614
Hacar, A., Alves, J., Burkert, A., & Goldsmith, P. 2016, A&A, 591, A104
Harris, C. R., Millman, K. J., van der Walt, S. J., et al. 2020, Natur, 585, 357
Hilder, T., Casey, A. R., Price, D. J., et al. 2025, ApJL, 984, L13
Hunter, J. D. 2007, CSE, 9, 90
Isella, A., Huang, J., Andrews, S. M., et al. 2018, ApJL, 869, L49
Izquierdo, A. F., Facchini, S., Rosotti, G. P., van Dishoeck, E. F., & Testi, L. 2022, ApJ, 928, 2
Izquierdo, A. F., Testi, L., Facchini, S., et al. 2023, A&A, 674, A113
Izquierdo, A. F., Testi, L., Facchini, S., Rosotti, G. P., & van Dishoeck, E. F. 2021, A&A, 650, A179
Koch, E., Ginsburg, A., AKL, et al. 2021, radio-astro-tools/radio-beam: v0.3.3, Zenodo, doi:10.5281/zenodo.4623788
Longarini, C., Lodato, G., Rosotti, G., et al. 2025, ApJL, 984, L17
Loomis, R., Facchini, S., Benisty, M., et al. 2025, ApJL, 984, L7
Miotello, A., Kamp, I., Birnstiel, T., Cleeves, L. C., & Kataoka, A. 2023, in ASP Conf. Ser. 534, Monograph 9: Protostars and Planets VII, ed. S. Inutsuka et al. (San Francisco, CA: ASP), 501
Paneque-Carreño, T., Izquierdo, A. F., Teague, R., et al. 2024, A&A, 684, A174
Pinte, C., Ilee, J. D., Huang, J., et al. 2025, ApJL, 984, L15
Pinte, C., Ménard, F., Duchêne, G., et al. 2018a, A&A, 609, A47
Pinte, C., Price, D. J., Ménard, F., et al. 2018b, ApJL, 860, L13
Pinte, C., Teague, R., Flaherty, K., et al. 2023, in ASP Conf. Ser. 534, Protostars and Planets VII, ed. S. Inutsuka et al. (San Francisco, CA: ASP), 645
Pinte, C., van der Plas, G., Ménard, F., et al. 2019, NatAs, 3, 1109
Rabago, I., & Zhu, Z. 2021, MNRAS, 502, 5325
Rosotti, G., Longarini, C., Paneque-Carreño, T., et al. 2025, ApJL, 984, L20
Stadler, J., Benisty, M., Izquierdo, A., et al. 2023, A&A, 670, L1
Stadler, J., Benisty, M., Winter, A. J., et al. 2025, ApJL, 984, L11
Teague, R., Bae, J., Aikawa, Y., et al. 2021, ApJS, 257, 18
Teague, R., Bae, J., Andrews, S. M., et al. 2022, ApJ, 936, 163
Teague, R., Bae, J., Bergin, E. A., Birnstiel, T., & Foreman-Mackey, D. 2018, ApJL, 860, L12
Teague, R., Benisty, M., Facchini, S., et al. 2025, ApJL, 984, L6
van der Velden, E. 2020, JOSS, 5, 2004
van der Walt, S., Schönberger, J. L., Nunez-Iglesias, J., et al. 2014, PeerJ, 2, e453
Virtanen, P., Gommers, R., Burovski, E., et al. 2020, scipy/scipy: SciPy v1.5.3, Zenodo, doi:10.5281/zenodo.4100507